

Research Article

Thermal Stability of Cryomilled Al-Mg-Er Powders

Bamidele Akinrinlola,¹ Raynald Gauvin,¹ Carl Blais,² and Mathieu Brochu¹

¹Department of Mining and Materials Engineering, McGill University, Montreal, QC, Canada H3A 0C5

²Department of Mining, Metallurgical and Materials Engineering, Laval University, Quebec City, QC, Canada G1V 0A6

Correspondence should be addressed to Bamidele Akinrinlola; bamidele.akinrinlola@mail.mcgill.ca

Received 4 May 2017; Accepted 17 August 2017; Published 28 September 2017

Academic Editor: Victor M. Castaño

Copyright © 2017 Bamidele Akinrinlola et al. This is an open access article distributed under the Creative Commons Attribution License, which permits unrestricted use, distribution, and reproduction in any medium, provided the original work is properly cited.

In this study, the thermal stability of nanostructured Al-Mg alloy powders was investigated. Two alloy compositions, Al-5Mg-0.1Er and Al-5Mg-0.5Er (wt.%), were cryogenically milled for 30 h to produce nanostructured powders. The microstructure of the milled powders with increasing temperature was investigated by differential scanning calorimetry (DSC) with one-hour annealing performed at selected temperatures followed by X-ray diffraction (XRD) and electron microscopy analysis. Prolonged milling led to significant oxygen pick-up in the powders. The Al-5Mg-0.1Er powders experienced grain growth typical of cryomilled Al-Mg powders, while the Al-5Mg-0.5Er alloy showed improved thermal stability. An average grain size of ~20 nm was observed up to 400°C (~0.8 T_m) in the Al-5Mg-0.5Er powders, and abnormal growth at 550°C resulted in a maximum observed grain size of 234 nm. Thermal stability in the Al-Mg-Er powders is attributed to the combined effects of solute/impurity drag and second-phase pinning (nanoscale oxides, nitrides, and oxynitrides) that impede grain boundary motion.

1. Introduction

Solute/impurities and nanoscale inclusions, such as nitrides and oxides introduced during the milling process, interfere with boundary mobility and reduce grain growth in milled Al alloy powders [1–4]. In order to improve grain size stability in milled Al alloy powders, research into the addition of alloying elements such as Sc has been conducted [5]. Sc exhibits slow diffusion kinetics in Al and forms nanoscale, coherent L1₂ trialuminide Al₃Sc precipitates that are able to pin grain boundaries and substructures [6]. Alloying with Sc shows some promise as seen with the delay of recrystallization in cryomilled Al-Mg-Sc powders [5]. Typically Sc additions give the most efficient improvement per weight percent added. Even though dilute (<0.12 at.%, 0.2 wt.%) additions are commonly made, the high cost of Sc (i.e., \$1400/100 g [7]) limits its widespread usage. Less costly trialuminide phase forming alternatives to Sc include lanthanide elements such as Er (\$540/100 g [7]). Additions of Er (<1 wt.%) to wrought Al-Mg series alloys have been investigated [8–11]. Similar to Sc effects, Er addition retards the recrystallization of deformed structures in Al-Mg alloys. However, limited studies at the nanocrystalline regime have been done to date.

In this work, the thermal stability of nanocrystalline Al-Mg-Er system (<1 wt.%, <0.1 at.% Er) was studied using differential scanning calorimetry (DSC), X-ray diffraction (XRD), and electron microscopy techniques.

2. Experimental

Atomized Al-Mg-Er powders were produced by the rotative electrode method at Laval University. Ternary compositions of Al-Mg-Er were cast into 10 cm length rods with 2 cm diameter. Samples were taken from top and bottom sections of the rods, and the composition of the cast rods was determined with the Inductively Coupled Plasma (ICP) technique using the Thermo Scientific iCAP 6500 Duo ICP-AES instrument. When the desired composition ranges were achieved, the rods were sent for atomization. Sieve analysis was used to determine the particle size distribution of the atomized powders and powders below 212 μm were selected for further use in this study. Both atomized powders had mode particle sizes of 106–150 μm. Composition of the powders was verified by ICP analysis and determined as Al-5.29Mg-0.12Er and Al-5.40Mg-0.55Er, in wt.% (as shown in Table 1); hereafter

TABLE 1: Composition of atomized and 30-hour milled powders (wt.%).

Element	Mg	Er	Ti	Fe	Ni	Tl	Si	Sb	Zn	Cr
Atomized 0.1 Er	5.29	0.12	0.19	0.07	0.01	0.15	0.07	0.05	0.04	0.00
Atomized 0.5 Er	5.40	0.55	0.06	0.04	0.00	0.04	0.07	0.01	0.02	0.00
Milled 0.1 Er	4.65	0.08	0.26	0.39	0.17	0.06	0.05	0.03	0.02	0.04
Milled 0.5 Er	4.48	0.44	0.01	0.16	0.03	0.00	0.05	0.01	0.02	0.03

these compositions will be referred to as 0.1 Er and 0.5 Er, respectively. Oxygen content of the powders was analyzed by SGS Canada Inc. by Instrumental Gas Analysis (IGA) and determined as 0.5 wt.% and 0.2 wt.% for the 0.1 Er and 0.5 Er powders, respectively.

The nanocrystalline Al-Mg-Er powders were produced by cryomilling in a Union Process HD-01 Lab Attritor with steel vial and grinding media at a speed of 300 rpm in liquid nitrogen. A two-stage milling process totaling 30 h was used: powders were first milled for up to 24 h and then remilled to a total 30 h. A ball to powder ratio (BPR) of 32:1 was used and a process control agent (0.25 wt.%) of stearic acid ($\text{CH}_3(\text{CH}_2)_{16}\text{CO}_2\text{H}$) was added to limit cold welding during milling. The particle size distribution was measured using a HORIBA LA-920 particle size analyzer. Mean particle size is $9.9 \mu\text{m}$ and $7.9 \mu\text{m}$ for 0.1 Er and 0.5 Er, respectively. After milling, the composition of the Al-Mg-Er powders was determined again by ICP and IGA. Composition of the powders was determined as Al-4.65Mg-0.08Er (0.1 Er) and Al-4.48Mg-0.44Er (0.5 Er), as shown in Table 1. Oxygen concentration in the milled powders was determined as 8.4 wt.% and 13 wt.% of oxygen for the 0.1 Er and 0.5 Er powders, respectively.

Differential scanning calorimetry (DSC) and thermogravimetric analysis (TGA) were conducted using the NETZSCH Simultaneous Thermal Analyzer STA 449 F3 instrument. Linear scans from 30°C – 750°C at $10 \text{ K}\cdot\text{min}^{-1}$ were run under flowing Ar atmosphere on samples ($\sim 40 \text{ mg}$) in alumina crucibles; empty crucible of alumina was used as reference. Powder samples were placed in alumina crucibles and heated to selected temperatures around DSC events at a rate of $10 \text{ K}\cdot\text{min}^{-1}$, isothermally held for one hour, and then cooled to room temperature. DSC scans were also conducted on samples ($\approx 15 \text{ mg}$) in alumina crucibles at 5 – $40 \text{ K}\cdot\text{min}^{-1}$ under flowing nitrogen atmosphere in a STARe DSC + TGA instrument.

XRD was performed using a Philips PW1710/00 Cu-K α source X-ray diffractometer, with a step size of $0.02^\circ 2\theta\cdot\text{s}^{-1}$. Alfa Aesar atomized pure Al powder (7 – $15 \mu\text{m}$ particle size) was annealed at 500°C for 2 h and used as the reference powder for peak analysis. Phases present in the powders were identified with the PANalytical X'Pert HighScore software. The lattice parameter of the powders was calculated from the peak positions with the XLPAT program, using Si powder as standard; XLPAT is a least squares program for the precise refinement of cell constants and is available online. The average grain size and strain in the powders were determined with the Method of Integral Breadths, using the FWHM values in place of the integral breadths after [12]; at least four Al reflections are used for the calculations.

X-ray photoelectron spectra were collected using the Thermo Scientific™ K-Alpha™ XPS spectrometer with an Al K α 1486.6 eV excitation source in a vacuum ($<5 \cdot 10^{-7}$ mbar) at room temperature. A minimum X-ray spot size of $40 \mu\text{m}$ was used. 8 scans were used for the valence, survey, and high resolution scans (i.e., Al2p, Mg1s, Er4d, Er4p, Cls, and O1s). A pass energy of 200 eV was used for the survey, while a pass energy of 50 eV was used for the valence and high resolution scans. The binding energies E_b were measured relative to the binding energy of Cls electrons on the sample surface accepted at 284.8 eV. Peak analysis is done using Shirley background removal. The milled powders were compacted into thin (1–2 mm thick) 2 cm diameter discs with a hydraulic press. The pressed powder was placed in a vacuum chamber for at least 24 hours before being transferred to a desiccator where the sample is stored until XPS analysis.

Analysis of the nanostructure was done with Scanning and Transmission Electron Microscopes (S/TEM): Hitachi SU8000, Philips CM200, and Tecnai G2 F20 instruments. TEM samples were prepared by dispersion of powders on a TEM Cu grid, and STEM samples by cold-mounting of powders in epoxy followed by thin slicing and preparation by ion-beam milling. Bright field (BF) and dark field (DF) images were used to obtain the grain size distributions; energy dispersive X-ray spectroscopy (EDS) analysis and selected area electron diffraction (SAED) patterns were used to determine the phases.

3. Results and Discussion

3.1. Atomized Al-Mg-Er Powders. As shown in Table 1, both powders contain similar levels of Mg in the atomized form, with 5.3–5.4 wt.% Mg. The Er content was determined to be approximately 0.12 wt.% for the 0.1 Er powder and 0.55 wt.% for the 0.5 Er powder. The content of impurity solutes in the atomized powders was reduced with increased Er addition. This trend has also been found in literature where the levels of Fe and Si impurity in a 5052 Al alloy were reduced by Er addition due to Er combining with Si and Fe in the melt [14]. XRD spectra of the atomized powders indicate an α -Al solid solution as shown in Figure 1; Si peaks are from the added crystallographic standard powder to correct peak position. Due to the higher concentration of Mg versus Er in the alloy, the changes in Al lattice parameter are attributed to the Mg solutes. Analysis of XRD peak shifts gives a lattice parameter of $\sim 4.0633 \text{ \AA}$ for both powders, which indicates approximately 4.5–4.6 at.% ($\sim 5 \text{ wt.}\%$) Mg is captured in solid solution. This is a marked improvement upon the equilibrium solubility in the Al-Mg system which is about 1 at.% Mg [15]. The data from XRD peak analysis of the atomized powders

TABLE 2: XRD results for atomized and 30 h milled powders.

Powder Condition	Lattice parameter (Å)	Mg in matrix (at.%)	Grain size, XRD (nm)	Microstrain (%)	Correlation coefficient, R^2	Grain size, TEM (nm)
Atomized, 0.1 Er	4.0633 ± 0.0011	4.52	37	0.048	0.91	—
Atomized, 0.5 Er	4.0637 ± 0.0003	4.62	67	0.059	0.92	—
Milled, 0.1 Er	4.0662 ± 0.0015	5.26	22	0.094	0.92	16 ± 1
Milled, 0.5 Er	4.0647 ± 0.0004	4.87	19	0.106	0.93	17

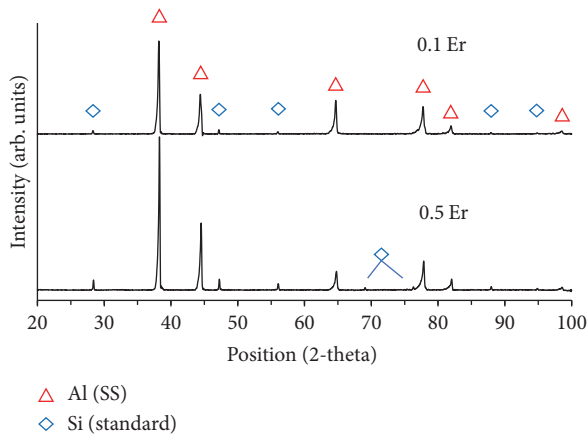


FIGURE 1: XRD spectra of atomized Al-Mg-Er powders.

are compiled in Table 2 including lattice parameter, solid solubility extension, minimum average crystallite size, and microstrain.

Backscattered SEM (BSE) images taken of the cross section of the atomized powders (Figure 2), show channeling contrast of the microstructure as well as the distribution of second phases in the powders. BSE images indicate that a range of micron to nanoscale grains is present in the atomized powders. Nanoscale grains are observed mostly around the edges of the atomized powders, an example of which is shown in Figure 2(c). XRD peak analysis also suggests the presence of nanocrystalline grains in the powders, with minimum crystallite sizes of 37 and 67 nm obtained in the 0.1 Er and 0.5 Er powders, respectively. Significant solute segregation is also present in the 0.5 Er powder. An EDS element line scan across areas of microsegregation in the 0.5 Er powders (inset of Figure 2(b)) indicates cosegregation of Er and Mg as shown in Figure 2(d). Low microstrain values are obtained in the powders, with 0.048% and 0.059% in the 0.1 Er and 0.5 Er powders, respectively. The powders have 0.5 wt.% and 0.2 wt.% oxygen content in the 0.1 Er and 0.5 Er compositions, respectively, which can be attributed to the nanoscale oxide film on the powder surfaces.

3.2. Cryomilled Powders. The composition of both powders is altered by the milling process as shown in Table 1. Changes in Mg and Er composition after milling in the 0.1 Er powders fall within the measurement uncertainty of the ICP technique. However, there is loss of Mg and Er content after milling in the 0.5 Er powder, likely due to oxidation during milling.

The increased Fe, Ni, and Cr content in both powders is a result of contamination from the milling equipment. After the two-stage milling procedure the powders contain 8.4 wt.% and 13 wt.% oxygen for the 0.1 Er and 0.5 Er milled powders, respectively. The significant oxygen levels in the final powders are attributed to oxygen pick-up in situ and after the cryomilling process. Similar results were reported by Goujon et al. [16] for mechanically alloyed 5000 Al/AlN powders prepared by cryomilling. Up to 10 wt.% oxygen was obtained in the powders after 25 h of milling in liquid nitrogen [16]. Increase in nitrogen contamination in the 5000 Al/AlN powders was also reported. Initial nitrogen content for a 5000 Al/AlN mixture with 20 vol.% AlN content is 7.2 wt.%; the nitrogen concentration increases linearly up to approximately 9.5 wt.% after 26 hours of milling. It is likely that similar levels of nitrogen contamination (~2 wt.%) are present within the powder samples studied here.

Figure 3 displays the XRD spectra of both 30 h milled powders, with peaks identified as the α -Al phase (Si is the standard) after cryomilling. Comparison of the α -Al peaks of the as-milled powders to those of atomized powders reveals (1) peak shifts to lower 2θ positions, indicating increased solubility from the starting condition, and (2) significant broadening, indicative of increased strain and grain refinement. Since the changes in the Al lattice parameter are attributed to the Mg solutes, the lattice parameters in this cryomilled Al-Mg-Er system are compared to those obtained for mechanically milled prealloyed Al-Mg powders to determine solid solubility extensions. The results of Scudino et al. [17] are used to estimate the Mg in solution for the milled powders. Data extracted from the diffraction patterns of the milled powders are compiled in Table 2 and grain size results from TEM image analysis are also included. Mg solubility in the matrix increases during the milling process. It is estimated that 5.26 at.% Mg and 4.87 at.% Mg are in solution in the 0.1 Er and 0.5 Er powders, respectively. Similar increases in solid solubility have been documented for other Al-Mg milled powder systems [3, 5].

An average minimum grain size of 22 nm and microstrain of 0.094% were determined for the 0.1 Er powder, while the 0.5 Er powder had a grain size of 19 nm and microstrain of 0.106%. The grain size and microstrain obtained are similar to those previously reported for milled Al and Al-Mg systems [1–3]. After 8 hours of milling, Zhou et al. observed an average grain size of 25 nm in Al-7.5Mg-0.3Sc (wt.%) alloy powders [5], with TEM analysis showing a heterogeneous milled microstructure consisting of nanocrystalline equiaxed grains as well as elongated lamellar-type grains. In comparison,

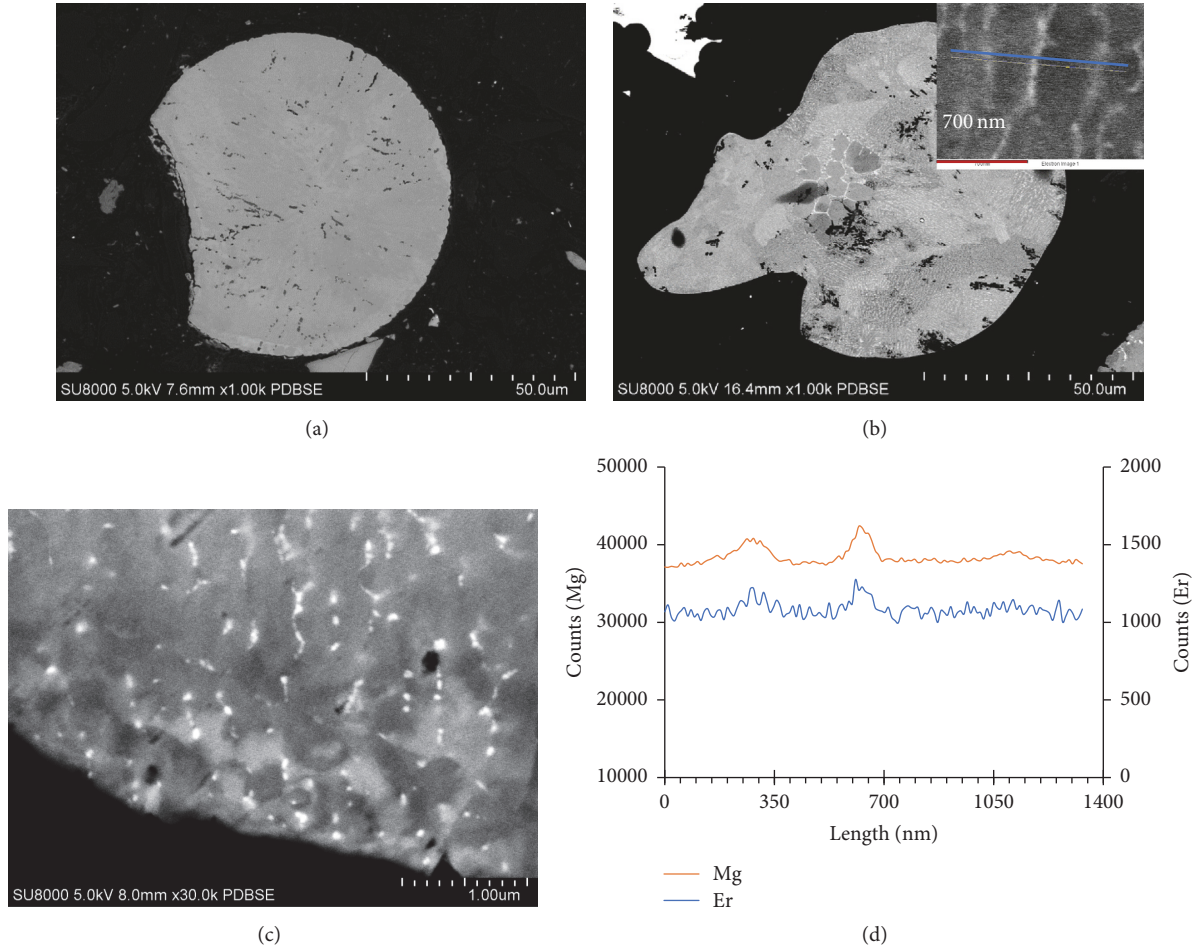


FIGURE 2: BSE images of atomized Al-Mg-Er powders: (a) 0.1 Er powder; (b) 0.5 Er powder with inset showing microscale segregation; (c) some nanoscale features in 0.5 Er powder; (d) EDS element line scan analysis from inset in (b) showing Mg and Er distribution.

TEM images of the as-milled powders in this study indicate only equiaxed nanocrystalline grains in the areas observed. Representative images are shown in Figures 3(b) and 3(c) with inset SAED patterns. The diffraction patterns contain rings which are indicative of nanocrystallinity and are indexed as the α -Al phase by the blue arcs in the images. Cryomilling studies performed by Zhou et al. on Al-Mg-Sc powders indicate that grain refinement in the alloy is of the same grain subdivision mechanism observed in Al and Al-Mg powders during the cryomilling process [18, 19]. It is proposed that similar refinement mechanisms take place in these Al-Mg-Er powders during milling. The average grain size is determined by TEM image analysis to be 16 ± 1 nm and 17 nm for 0.1 Er and 0.5 Er, respectively. The grain size distribution, shown in Figure 3(d), indicates that 85% of the grains are below 30 nm for both samples; the frequency is shown on the left vertical axis, while the cumulative frequency curve corresponds to the right axis.

The thickness and composition of the oxide film, as well as the hydroxide film, are determined via XPS analysis of the surface layers of the milled powders. The average thickness of the oxide film is estimated from the intensities of the Al2p

peaks obtained from the powders with the following equation from [5, 20]:

$$d = \lambda_o \sin \theta \ln \left[\frac{C_m \lambda_m I_o}{C_o \lambda_o I_m} + 1 \right], \quad (1)$$

where I_m and I_o are the intensities (i.e., peak areas) of the metal and oxide photoelectron peaks, respectively; C_m and C_o are the volume densities of metal atoms in the metal and oxide, respectively, taken as $100.14 \text{ mole}\cdot\text{dm}^{-3}$ for Al metal and $71.85 \text{ mole}\cdot\text{dm}^{-3}$ for the oxide from [21]; λ_m and λ_o are the inelastic mean free paths (IMFPs) of the photoelectrons in the metal and oxide, respectively (in Å); d is the oxide thickness (in Å); and θ is the electron take-off angle (with respect to the sample surface). The use of effective attenuation lengths (EALs) rather than IMFPs is suggested since they take into account the effect of elastic scattering [22]. Average EAL values are taken as $\lambda_m = 2.39$ and $\lambda_o = 2.92$ from [22]. Fitting of the O1s, Al2p, Mg2p, and valence bands is shown in Figure 4.

The Al2p peaks for both powders are shown in the first row of Figure 4. The oxide film is calculated as 52 Å (5.2 nm) for the 0.1 Er powder and 59 Å (5.9 nm) for the 0.5 Er. The

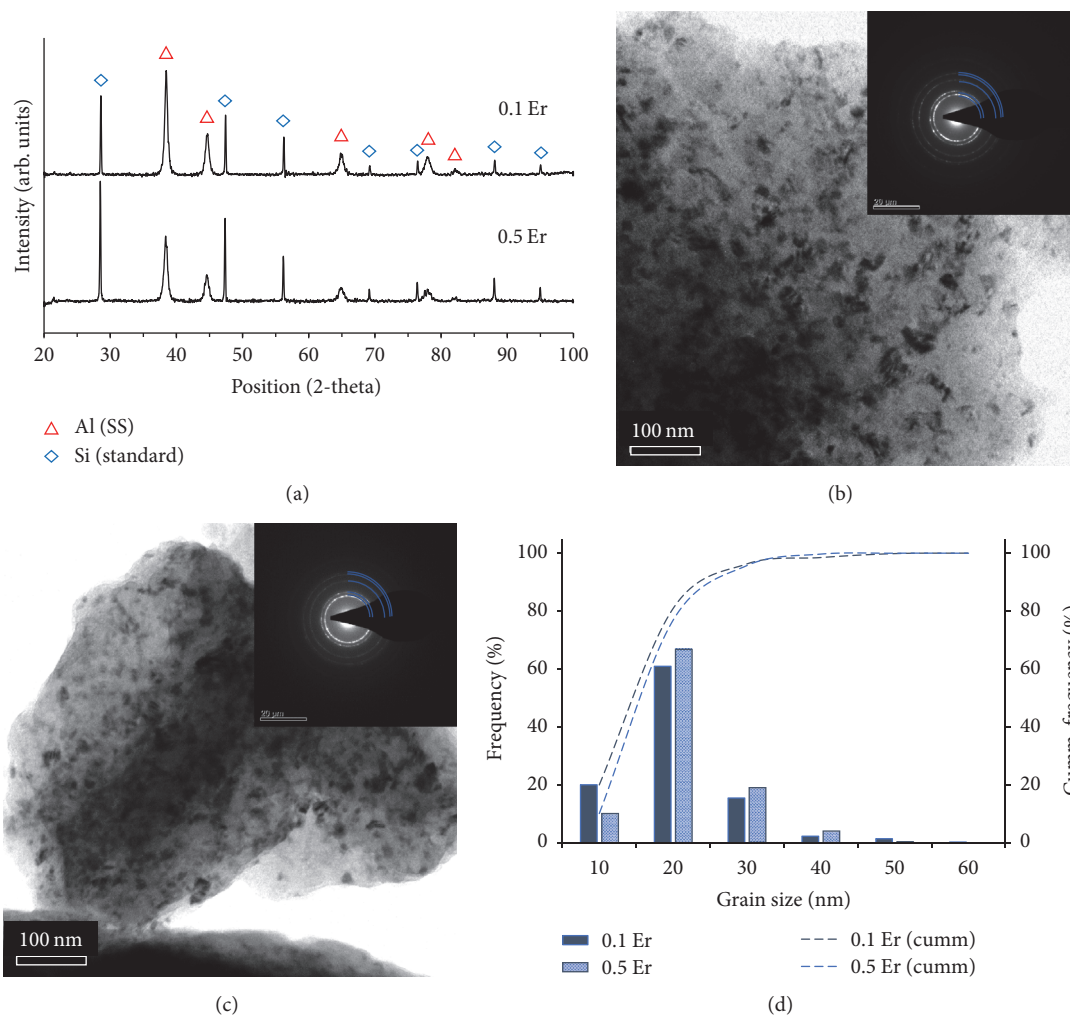


FIGURE 3: 30 h milled powders with supersaturated α -Al phase after milling (a); nanocrystalline grains as shown in Bright field TEM images of 0.1 Er (b) and 0.5 Er (c), both with inset SAED patterns taken from the areas shown; and the grain size distributions obtained from TEM image analysis (d). The nanocrystalline α -Al phase is indicated by the blue arcs.

thickness of the oxide films on the powders is also assessed from TEM micrographs of the powders as shown in Figure 5. The oxide measured in the HRTEM micrograph of the 0.1Er powder agrees with the XPS measurement, with a thickness of ~ 4 nm measured. However, the 0.5 Er powder shows varying oxide thickness, with thickness ranging within ~ 5 –10 nm at various areas of the powder surface. The thickness of the hydroxide layer is estimated using the ratio of the OH^- peak area to the total O peak area. Results of hydroxide layer and composition calculations are summarized in Table 3. The hydroxide film on the 0.5 Er showed a slight increase compared to the 0.1 Er powders, changing from a ratio of 17% to 19%. Composition of the oxide film is determined from the intensities of the $\text{Al}2p$ and $\text{Mg}2p$ peaks. The 0.1 Er powder is estimated to have approximately 3% Mg in the oxide layer, while 0.5 Er has 4% Mg.

3.3. DSC Analysis of Milled Al-Mg-Er Powders. The $10 \text{ K}\cdot\text{min}^{-1}$ DSC scans from 30°C to 750°C of both milled powders are shown in Figure 6. According to FactSage

calculations for the Al-5Mg-(0.1–1)Er system (wt.%), the bulk solidus and liquidus temperatures are approximately 575°C and 635°C , respectively; therefore it is assumed that events prior to 575°C are unique to the microstructure of the powders. The scans here show exothermic events at approximately 160°C (A) and 475°C (B), with bulk melting events at 650°C (C).

Milled Al-Mg systems typically exhibit recovery or grain boundary restructuring events below 200°C [3–5]. A study on the thermal behavior of milled 5083 powder identified a grain boundary reordering event at approximately 158°C [4], while recovery events were observed around 164°C in milled Al-7.6Mg (at.%) [3] and 172°C in Al-7.5Mg-0.3Sc (wt.%) [5]. These results suggest that the event marked (A) is a recovery event. Although both milled Al-7.6Mg (at.%) and Al-7.5Mg-0.3Sc (wt.%) exhibited recrystallization events around 330°C [3, 5], no exothermic peaks are observed in either DSC trace around this temperature range. The study on milled Al-7.5Mg-0.3Sc reported an exothermic peak at approximately 450°C , which was interpreted as a precipitation peak for the

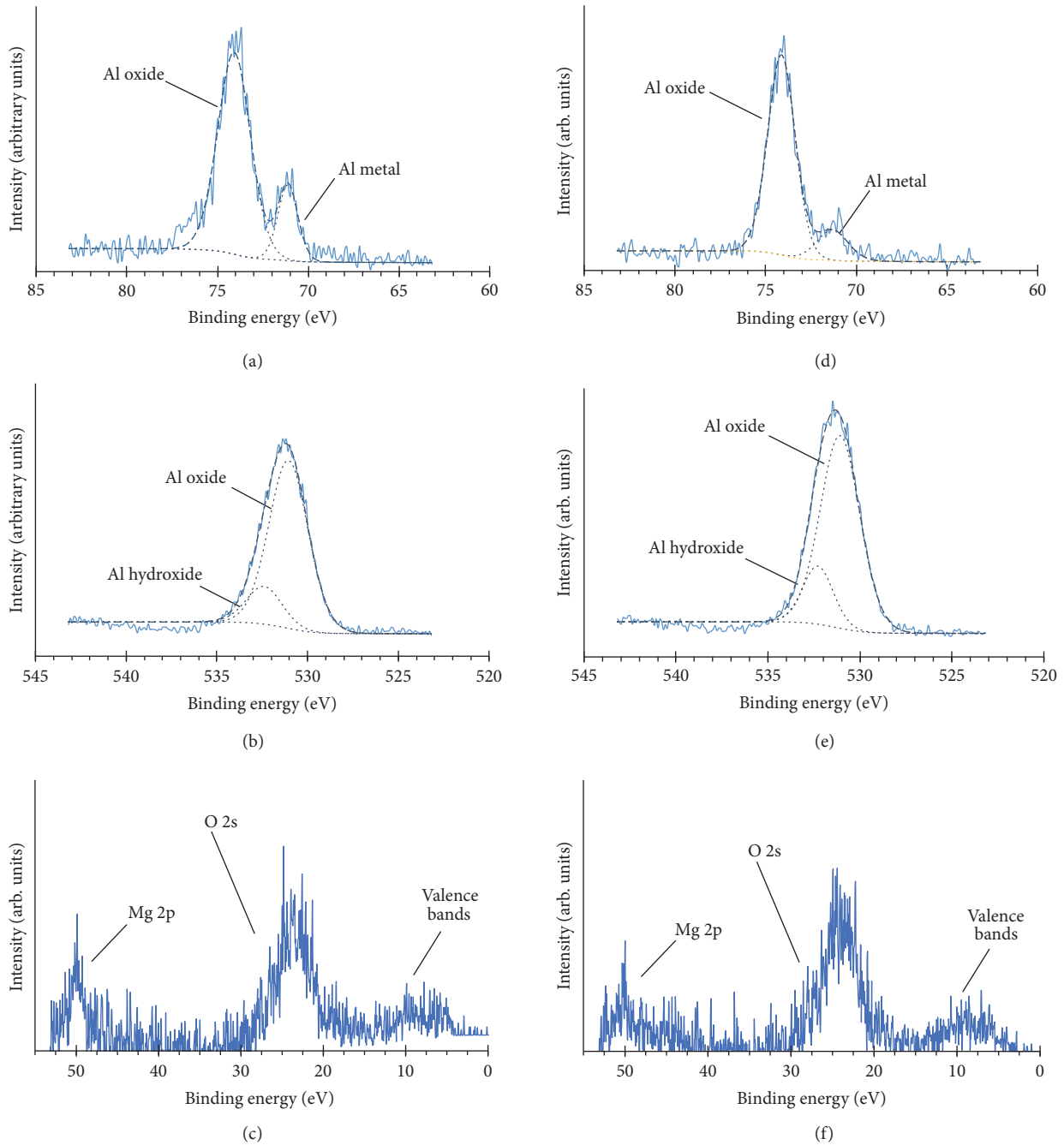


FIGURE 4: XPS analysis of oxide film on 0.1 Er (a–c) and 0.5 Er powders (d–f): Al2p peaks (a, d); O1s peaks (b, e); valence region with Shirley background subtracted (c, f).

Al_3Sc phase [5]. However, the weight gain observed here in the TG curve, starting at 350°C , suggests that exothermic peak B is an oxidation event. Similarly, TG tests on cryomilled Al-7.6Mg powders have shown the onset of oxidation in milled powders beginning at 350°C [3]. Another study on the oxidation behavior of milled Al-Mg powders with compositions ranging from $\text{Al}_{0.95}\text{Mg}_{0.05}$ to $\text{Al}_{0.5}\text{Mg}_{0.5}$ has shown that oxidation proceeds in two stages in an oxygen atmosphere with the onset of oxidation observed over the range of $525\text{--}570^\circ\text{C}$ due to the selective oxidation of Mg [23].

Oxidation of Al-rich Al-Mg alloys at high temperatures is dependent on the Mg and oxygen diffusion through the amorphous oxide layer and subsequent reactions at the oxide-gas and oxide-metal interfaces. The oxide films which developed on an Al-4.2 wt.% Mg at high temperatures consisted of two types of MgO, primary and secondary oxides, which were dependent on the mechanism of formation [24]. Primary oxidation is the direct reaction at the oxide/metal interface between Mg from the alloy substrate with oxygen to form MgO. Secondary oxidation is the solid-state reduction of

TABLE 3: Oxide composition from XPS peak analysis.

Powder	Thickness, XPS (Å)	Al2p	Mg2p	OH ⁻ / [O ²⁻ + OH ⁻]
0.1 Er	52	0.97	0.03	0.17
0.5 Er	59	0.96	0.04	0.19

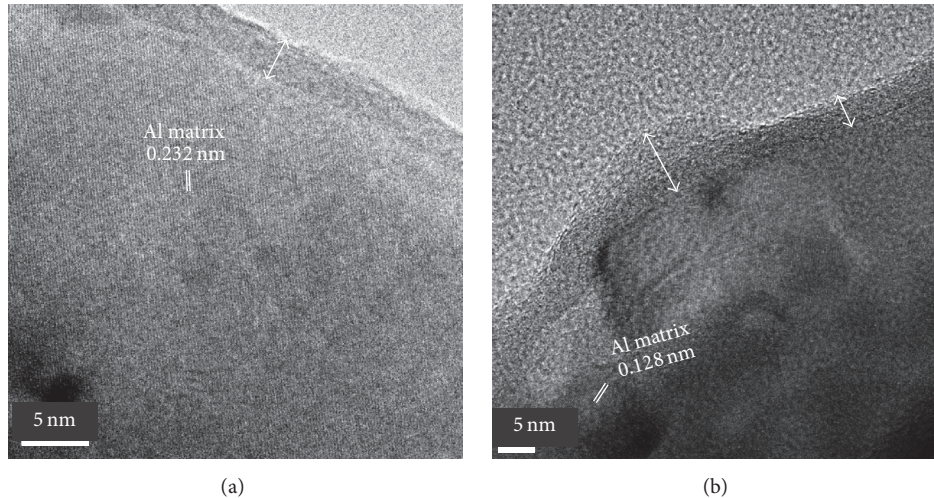
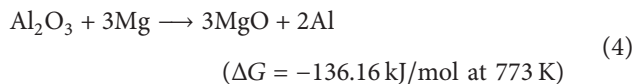
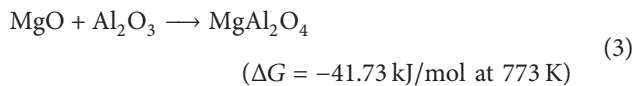
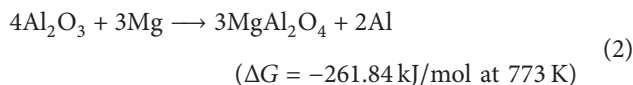


FIGURE 5: HRTEM images of (a) 0.1 Er and (b) 0.5 Er powders showing the oxide film (indicated by arrows) and the crystalline Al matrix: $d \approx 0.232$ nm ($d_{111} = 0.23379$ nm) and $d \approx 0.128$ nm ($d_{311} = 0.12209$ nm).

the original air-formed amorphous γ -Al₂O₃ film by Mg from the alloy substrate to form MgO [24]. Although the powder annealing is done under a flowing Ar atmosphere, complete removal of oxygen from the DSC chamber is not assured. Therefore, there is the possibility of both primary and secondary oxidation occurring during the DSC run and subsequent annealing processes.

Crystalline spinel phases could be formed by reduction reactions—(1) between Mg and the nanoscale oxides inside the milled powder and (2) between Mg and the oxide film at particle surfaces. Spinel and periclase (MgO) particles can form from several solid-state reduction reactions [25]:



Spinel formation due to solid-state reactions between the periclase and alumina particles will be dependent on the proximity of the MgO particles to the alumina oxide film/particles within the powders. The diffusivity of Mg will also affect the reduction reactions. Spinel formation is more thermodynamically favored to form at 500°C as seen in the reactions presented above.

One-hour annealing is carried out to determine the nature of the events observed during the scans, up to 580°C.

Temperatures are chosen at points before/after and during events (A), (B), and (C). Temperatures are 150°C, 180°C, 250°C, 330°C, 500°C, and 580°C for the 0.1 Er powder, while 150°C, 250°C, 400°C, 450°C, 500°C, and 580°C are selected for the 0.5 Er powder. XRD patterns are collected after each anneal and the microstructure is also observed by TEM. The results of the annealed 0.1 Er powders will be presented in the next section of this chapter and the 0.5 Er results in the subsequent section.

3.4. Annealing Behavior of 0.1 Er Powder

3.4.1. XRD Results of 0.1 Er Powder. Normalized XRD patterns of the as-milled and annealed 0.1 Er powders are presented in Figure 7. The lattice parameter, estimated Mg in solid solution, grain size, and microstrain calculated from the XRD patterns are summarized in Table 4; the average grain size from TEM image analysis is also included. Grain size distributions from annealing at selected temperatures are shown in Figure 8; the largest grain size observed at each temperature is also included in the figure.

The major phase observed in the powders, marked in Figure 7, is the α -Al phase. At 500°C and 580°C, peaks associated with the MgAl₂O₄ spinel phase are also identified indicating the formation of crystalline oxide phases. Shifting of the α -Al peak positions indicates changes in the Mg solubility with increasing temperature. Milling created a supersaturated solid solution of 5.26 at.% Mg in the matrix, which decomposed after low temperature annealing. After annealing at 150°C, the estimated Mg in the matrix is 3.05 at.%, higher than the equilibrium value of ≈ 2.5 at.%

TABLE 4: XRD results and TEM grain size for the 0.1 Er annealed powders.

Powder sample	Lattice parameter (Å)	Mg in matrix (at.%)	Grain size, XRD (nm)	Microstrain (%)	Correlation coefficient, R^2	Grain size, TEM (nm)	Number of grains, N
Milled	4.0662 ± 0.0015	5.26	22	0.094	0.92	16 ± 1	592
150°C	4.0575 ± 0.0004	3.05	24	0.041	0.97	23 ± 1	325
180°C	4.0537 ± 0.0007	2.08	26	0.09	0.97	32 ± 3	313
250°C	4.0549 ± 0.0002	2.39	32	0.076	0.99	32 ± 3	318
330°C	4.0552 ± 0.0002	2.46	34	0.052	0.95	37 ± 4	665
500°C	4.0538 ± 0.0004	2.11	50	0.087	0.86	45 ± 5	390

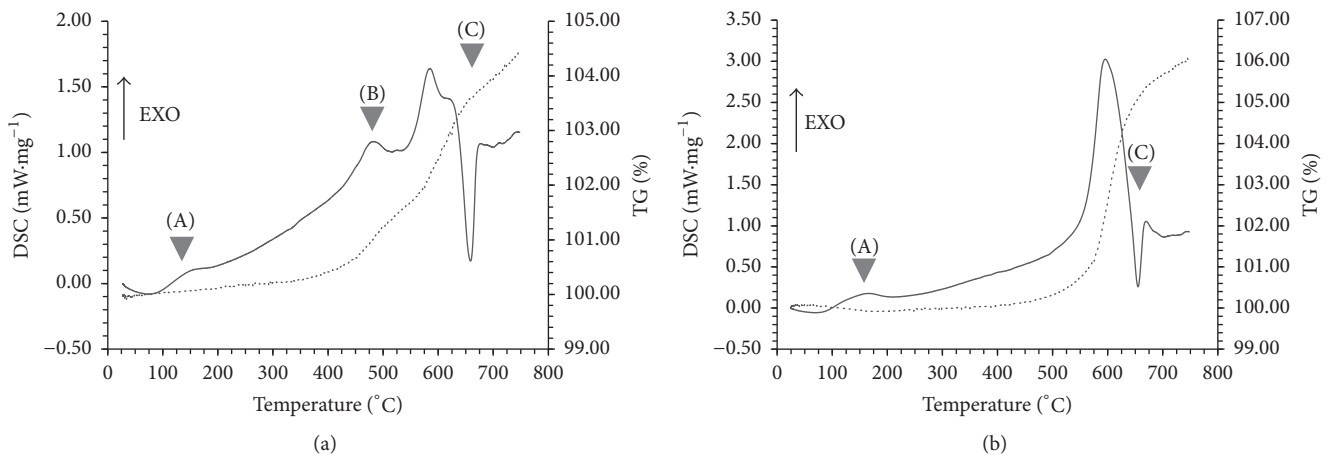
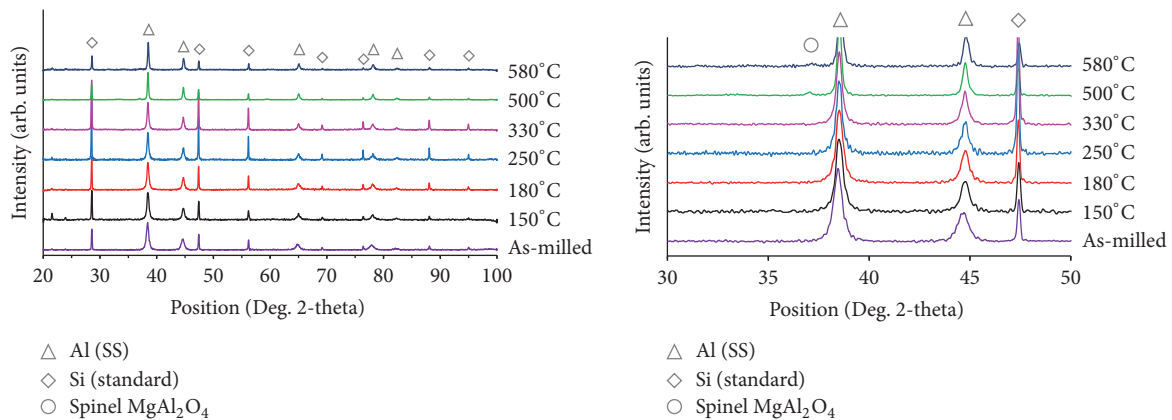
FIGURE 6: DSC traces (solid lines) and TG traces (dotted lines) of 0.1 Er and 0.5 Er powders at heating rate of $10 \text{ K}\cdot\text{min}^{-1}$ under flowing Ar: exothermic events (A) and (B) and endothermic event (C).

FIGURE 7: XRD patterns of the annealed 0.1 Er powders with major phases labelled, 25 to 60 Deg. 2-Theta inset shows minor crystalline oxide peaks.

observed in the Al-Mg phase diagram [15]. At 180°C, the matrix content further reduces to 2.08 at.% and remains fairly constant thereafter with increasing annealing temperature, where 2.11 at.% is still in solution after the annealing at 500°C. Decreasing Mg supersaturation without the appearance of β or β' phase reflections in the XRD patterns suggests low volume of second-phase precipitates but could also be an

indication of Mg segregation to the grain boundary. Straumal et al. [26] found that partial decomposition of supersaturated solid solutions in Al-5Mg and Al-10Mg alloys after high pressure torsion (HPT) at room temperature resulted in nanoscale β precipitation (of less than 1 vol.%). However, Sauvage et al.'s study of an Al-5.7Mg-0.4Mn-0.32Sc (wt.%) alloy processed by HPT showed that decomposition of the

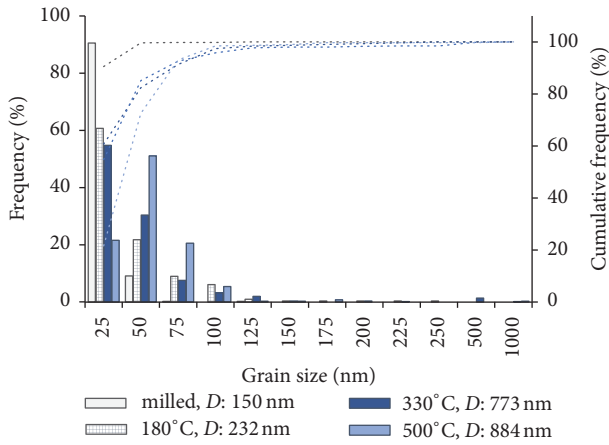


FIGURE 8: Grain size distributions obtained from TEM image analysis for selected 0.1 Er annealed powders. D is the largest grain size observed at temperature.

solid solution and segregation of Mg clusters to the grain boundary occurred during processing at room temperature and 200°C [27].

General sharpening of the α -Al peaks from the as-milled state with increasing temperature is indicative of (1) reducing microstrain in the powders and (2) increasing crystallite/grain size. XRD analysis indicates a linear increase in the average grain size from 22 nm in the as-milled powder to a grain size of 50 nm at 500°C. However, the microstrain in the 0.1 Er powder exhibits unexpected trends. Although the annealing at 150°C resulted in reduced microstrain to 0.041%, similar values are obtained in the as-milled condition and at 180°C at 0.094% and 0.09%, respectively. Additionally, the microstrain increases from 0.052% at 330°C to 0.087% after annealing at 500°C.

The uncharacteristic changes in microstrain could be due to nonhomogeneous solute distributions in the milled powders. Peak broadening due to solute effects as well as grain size and microstrain contributions was observed in milled Ni-15 at.% W powder [28]. Rane et al. [28] concluded that concentration inhomogeneity affected the microstrain obtained from the annealed Ni-W powders. Fluctuating microstrain values were obtained in the milled Ni-W powders with increasing temperature and annealing time. This behavior was attributed to lattice broadening due to inhomogeneous distribution of W solutes in the Ni grains that may overshadow strain reduction resulting from microstructural relaxations. It is possible that similar conditions may occur in these milled Al-Mg-Er powders, where inhomogeneous distribution of Mg in the Al grain matrix may contribute to the variations in microstrain obtained from the annealed powders.

3.4.2. TEM Results of 0.1 Er Powder. Although some changes in the grain size distribution occur at 150°C, significant grain growth (normal and abnormal) is not observed until 180°C. As shown in Figure 8, 90% of the grains remain below 100 nm

at 180°C and there is growth into the UFG regime as seen with the largest grain size of 232 nm observed. The average grain size from TEM analysis changes from 16 ± 1 nm to 23 ± 1 nm to 32 ± 3 nm for powder as-milled, at 150°C and at 180°C, respectively, which agrees well with the grain sizes obtained from XRD.

The microstructure evolution in annealed 0.1 Er powders is presented in Figure 9. Figures 9(a) and 9(b) show the typical nanocrystalline regions in the powders annealed at 150°C and 180°C, respectively; the diffraction rings in the inset SAED patterns are characteristic of the nanocrystalline structure. Other areas in the 0.1 Er powders annealed at 180°C exhibit a bimodal microstructure with a representative image shown in Figure 9(c). Similar to the microstructure of the powders annealed at 250°C, powders annealed at 330°C exhibit abnormal grain growth with large ultrafine grains nestled within nanocrystalline regions; images representative of the microstructure at 330°C are shown in Figures 9(d) and 9(e). The average grain size from TEM analysis is constant at an average of 32 nm (within standard deviation) from 250°C to 330°C, which agrees well with the XRD results. However, the largest observed grain diameter continues to increase from 232 nm at 250°C up to 773 nm at 330°C. The grain size distribution changes significantly at 500°C when the mode size shifts to 25–50 nm, as seen in Figure 8. From TEM image analysis, the average grain size increases from 37 ± 4 nm at 330°C to 45 ± 5 nm at 500°C, with the maximum grain size growing closer to 1 μ m (Figure 9(g)).

SAED patterns from the larger grained areas shown in Figure 9 are presented in Figure 10. The diffraction patterns contain diffraction spots consistent with single crystals and rings indicating the presence of nanoscale second phases in the regions. Evidence of second phases is only observed in areas with grain sizes larger than 100 nm. The main spot diffraction patterns are indicated by small circles, while the diffraction rings are indicated by the arrows in the figures. The spot diffraction patterns correspond to Al crystals imaged from the $\bar{1}03$ direction (Figure 10(a)), the $[112]$ direction (Figure 10(b)), and the $[121]$ direction (Figure 10(c)). Second phases observed in some of the large grains in powders annealed at 330°C are shown in Figure 10(d). The lattice spacing corresponding to the diffraction rings from the SAED patterns in Figure 10 are calculated as $d \approx 2.09$ Å and $d \approx 1.49$ Å.

Although nanoscale Al_3Sc precipitates were observed in a milled Al-Mg-Sc powder after annealing at 200°C [5] and studies on the precipitation behavior of Al_3Sc indicate that Mg addition may accelerate the formation of these precipitates [29], the SAED patterns of Figure 10 do not exhibit the characteristic $\text{L}1_2$ superlattice reflections. Also DSC and TEM studies on precipitation in coarse grained Al-16Mg alloys by Starink and Zahra [30, 31] have identified temperatures 180°C–290°C as the temperature range for β' precipitation. And the study by Straumal et al. [26] showed that a small fraction of nanoscale β precipitates formed in room temperature by HPT formed nanograined Al-5Mg and Al-10Mg alloys. However, the diffraction rings observed here would correspond to peaks of lower intensity, while the highest intensity ring (i.e., $d = 2.395$ Å) is absent.

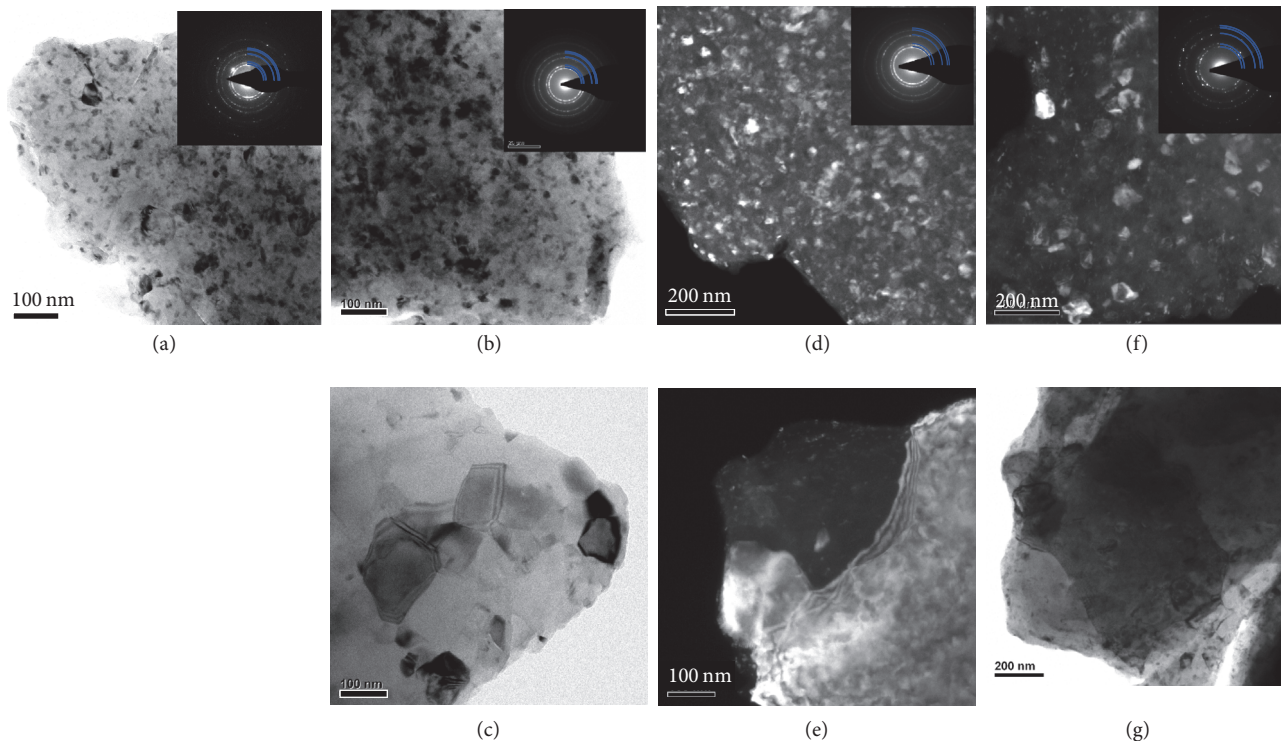


FIGURE 9: TEM images of 0.1 Er powder annealed at 150°C (a), 180°C (b, c), 330°C (d, e), and 500°C (f, g); top row: nanocrystalline regions; bottom row: abnormal grain growth. Nanocrystalline α -Al phase is indexed with the blue arcs.

The lattice measurements of Figure 10 can be indexed to the 200 ($d = 2.11 \text{ \AA}$) and 220 ($d = 1.492 \text{ \AA}$) planes of the MgO phase. In previous studies, Mg(O,N) dispersoids have been observed in an UFG Al-Mg-Sc alloy produced by milling and ECAP consolidation [32]. Results of STEM analysis of the milled powders annealed at 330°C also indicate the presence of some Al-Mg-O (~30–40 nm) phases as shown in Figure 11. These results suggest that the nanoscale particles observed after annealing at 180°C, 330°C, and 500°C are likely nanoscale MgO particles. Al-Fe phases (~80 nm) phases were also observed in the powders, also shown in Figure 11. The Al-Fe precipitates observed in the powders could correspond to the Al_6Fe phase. Nanoscale precipitates of the metastable Al_6Fe phase were observed after one hour of annealing at 330°C, and both Al_6Fe and the equilibrium phase $\text{Al}_{13}\text{Fe}_4$ after annealing at 500°C in a milled $\text{Al}_3\text{Fe}_3\text{Cr}_2\text{Ti}_2$ alloy [33]. At 370°C, the Al_6Fe particles were 15–30 nm in size, increasing to 15–50 nm after annealing at 450°C.

3.5. Annealing Behavior of 0.5 Er Powder

3.5.1. XRD Results of 0.5 Er Powder. Normalized XRD patterns of the as-milled and annealed 0.5 Er powders are presented in Figure 12. The lattice parameter, estimated Mg in solid solution, grain size, and microstrain calculated from the XRD patterns are summarized in Table 5; average grain sizes from TEM image analysis are also included in the table. Grain size distributions after annealing at selected temperatures are shown in Figure 13; the largest grain size observed at each

temperature is also given in the figure. The major phase in the powders, marked in Figure 12, corresponds to the α -Al phase. Reflections from the MgAl_2O_4 spinel phase are identified at 500°C and 580°C.

General sharpening of the α -Al peaks from the as-milled state with increasing temperature is indicative of (1) reducing microstrain in the powders and (2) grain growth. Shifts in the peak positions are observed indicating changes in the Mg solubility. The milling process created a supersaturated solid solution of Mg in the matrix of 4.87 at.%. With increasing temperature, there is decomposition of the solid solution and reducing Mg in the matrix. At 150°C, the Mg in the matrix is estimated to reduce to 2.72 at.%, approximately the equilibrium solubility of ~2.5 at.% Mg [15]. With further annealing at higher temperatures, the Mg content in the matrix approaches ~2 at.%. From the as-milled state till annealing at 450°C, the average grain size remains below 30 nm in the 0.5 Er powder. However, a grain size of 41 nm is obtained at 500°C, similar to the findings in the 0.1 Er powder at high temperature.

The microstrain decreases in the 0.5 Er powder after annealing, from 0.106% in the as-milled state to 0.066% after annealing at 150°C. The microstrain is ~0.06% until annealing at 450°C when it increases. A microstrain of 0.089% is then obtained at 450°C, before reducing to 0.078% at 500°C. As can be observed in Table 5, the microstrain in the powder increases as the Mg content in the matrix increases with temperature. The Mg content in the matrix increases with the solid solubility limit of the Al-Mg system, which increases

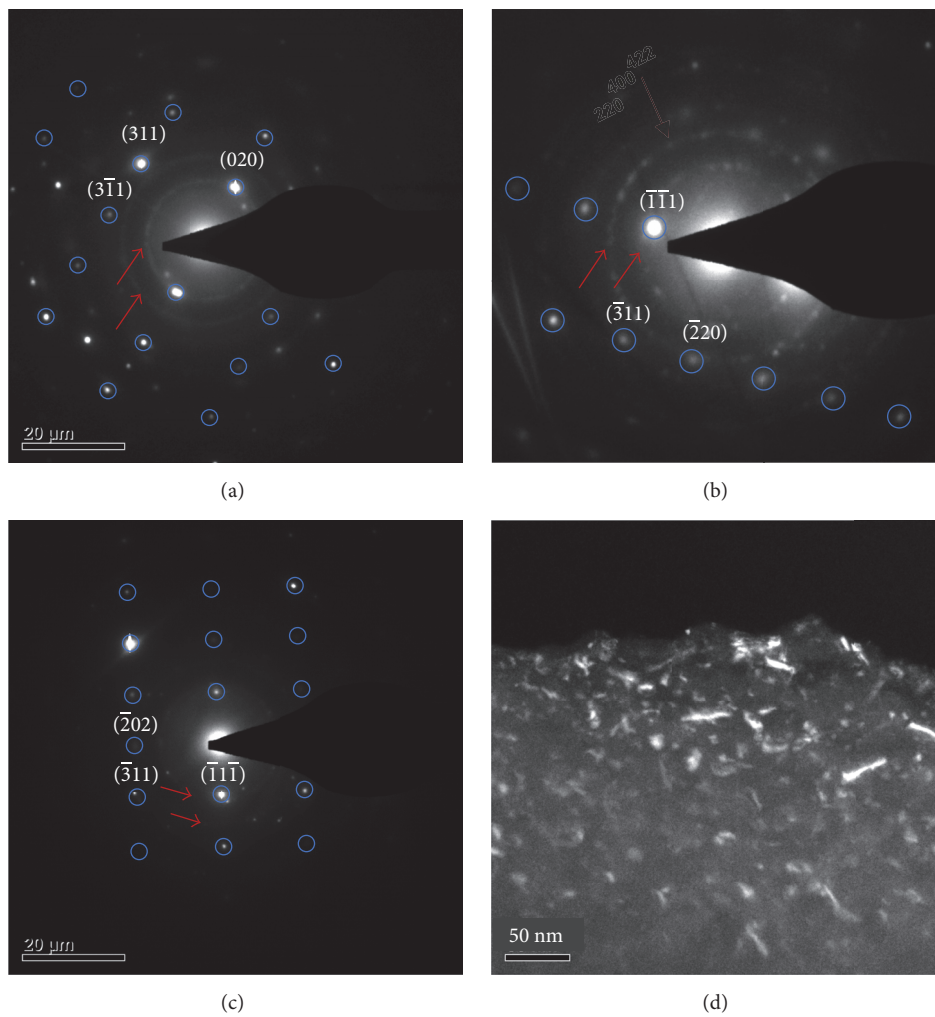


FIGURE 10: Indexed SAED patterns from the large grained regions shown in Figure 9: Al grains viewed from (a) $\mathbf{B} = [\bar{1}03]$ direction at 180°C, (b) $\mathbf{B} = [112]$ direction at 330°C, and (c) $\mathbf{B} = [121]$ direction at 500°C; (d) second-phase particles observed in powders annealed at 330°C. The small circles indicate the spot diffraction pattern and rings (indicated by arrows) are produced by nanoscale phases in the imaged regions.

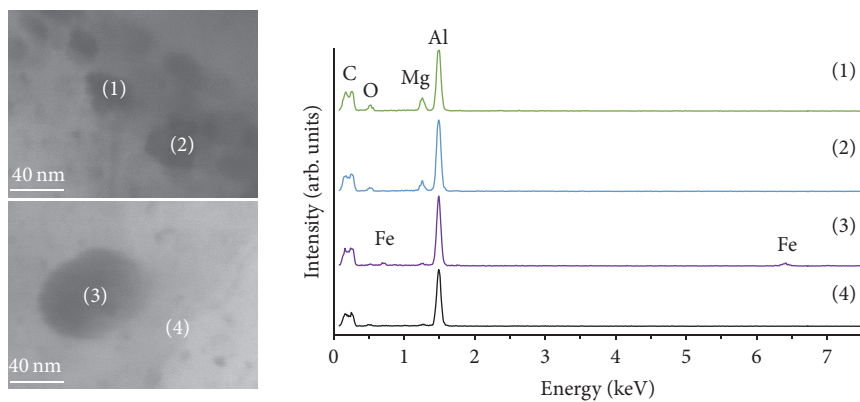


FIGURE 11: Nanoscale phases observed in the powders annealed at 330°C are identified by numbers 1 through 4 and similarly numbered corresponding STEM-EDS analysis.

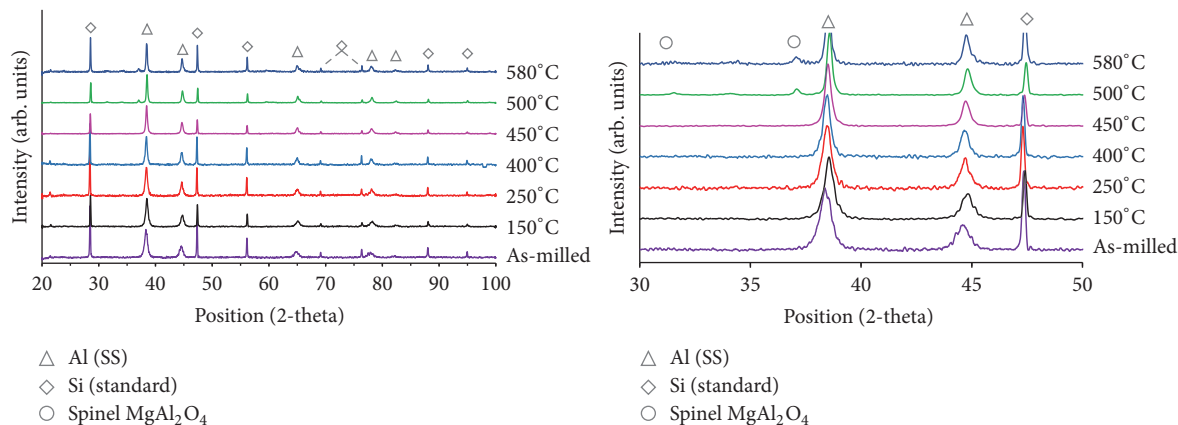


FIGURE 12: XRD patterns of the annealed 0.5 Er powders with major phases labelled, 25 to 60 Deg. 2-Theta inset showing minor crystalline oxide peaks.

TABLE 5: XRD results and TEM grain size for the 0.5 Er annealed powders.

Powder sample	Lattice parameter (Å)	Mg in matrix (at.%)	Grain size, XRD (nm)	Microstrain (%)	Correlation coefficient, R^2	Grain size, TEM (nm)	Number of grains, N
Milled	4.0647 ± 0.0004	4.87	19	0.106	0.93	17 ± 0	657
150°C	4.0562 ± 0.0025	2.72	21	0.066	0.89	22 ± 1	468
250°C	4.0519 ± 0.0004	1.62	23	0.054	0.94	18 ± 1	372
400°C	4.0530 ± 0.0006	1.90	27	0.06	0.97	18 ± 1	328
450°C	4.0544 ± 0.0006	2.26	35	0.089	0.93	32 ± 2	301
500°C	4.0537 ± 0.0005	2.08	41	0.078	0.85	54 ± 4	300

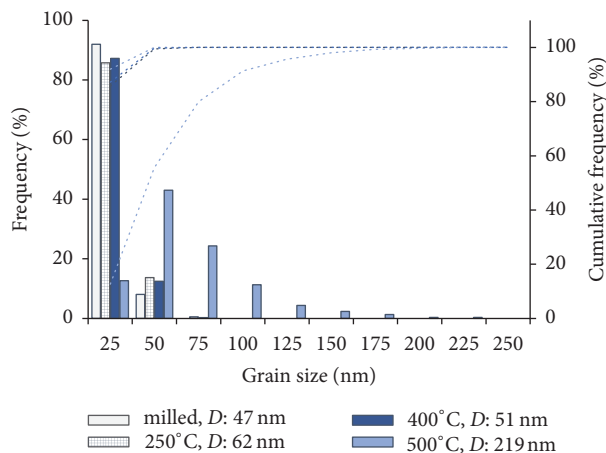


FIGURE 13: Grain size distribution obtained from TEM image analysis for selected 0.5 Er annealed powders. D is the largest grain size observed at temperature.

from ~ 1 at.% at room temperature to 18.9 at.% at 450°C. It is possible that the increase of Mg in the matrix also contributes to the changes observed in the microstrain, in addition to possible effects from inhomogeneous Mg distribution within the powders.

3.5.2. TEM Results of 0.5 Er Powder. XRD analysis of the 0.5 Er powder indicated an increase in the average grain size after the first DSC event from 19 nm in the as-milled powder to 23 nm at 250°C. However, TEM image analysis reveals that grain size distributions at 150°C and 250°C are identical to the as-milled condition, with more than 95% of the grains remaining below 100 nm as shown in Figures 13 and 14; the average grain size remains at 18 ± 1 nm average. SAED patterns taken from the nanostructure indicate only the α -Al phase. Extra reflections from nanoscale second-phase precipitates are not observed in the diffraction patterns.

TEM image analysis indicates the grain size distribution remains constant and the average is 18 ± 1 nm up to 400°C, with onset of appreciable growth (normal and abnormal) at 450°C. The average grain size roughly doubles to 32 ± 2 nm and the maximum grain size at 450°C is 280 nm. As seen in Figure 13, the mode grain size changes at 500°C, with grain growth in the ultrafine regime. TEM images of powders annealed at 400°C, 450°C, and 500°C are presented in Figure 15. The nanocrystallinity at 400°C can be seen in Figure 15(a), while the onset of abnormal grain growth at 450°C is shown in Figure 15(b), the increase in grain size at 500°C is shown in Figure 15(c) with the accompanying SAED pattern shown in Figure 15(d). SAED patterns taken at 500°C indicate the presence of the α -Al (blue arcs) and MgAl_2O_4 spinel phases.

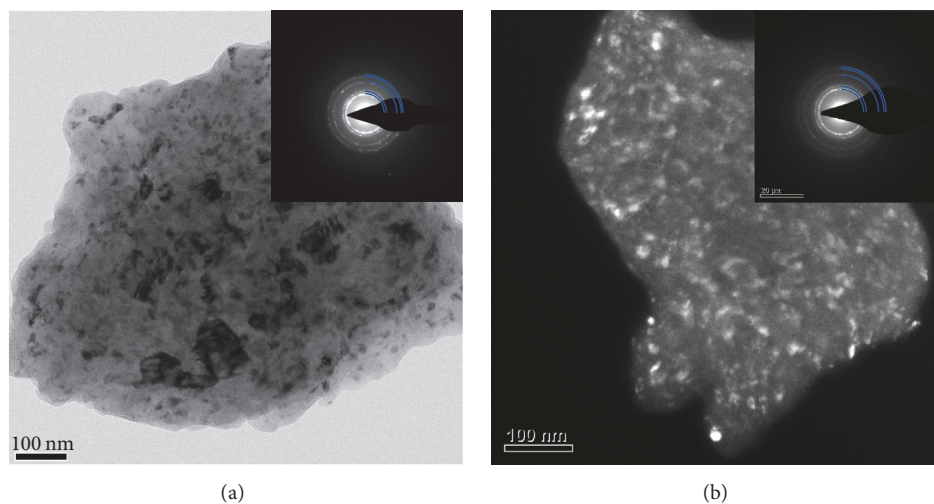


FIGURE 14: Nanocrystalline grains after annealing of 0.5 Er powders at 150°C (a) and 250°C (b). Nanocrystalline α -Al phase is indexed with blue arcs.

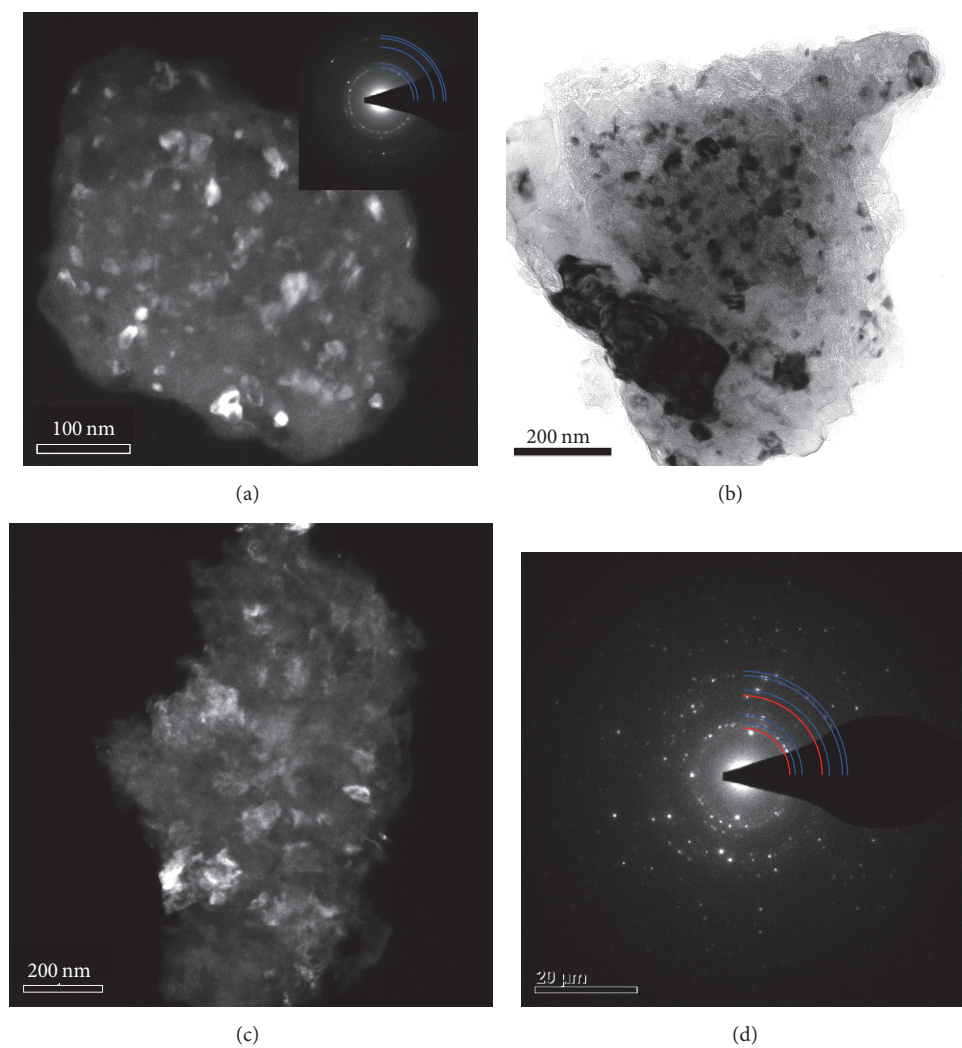


FIGURE 15: TEM images of the 0.5Er powders after various annealing: nanocrystalline regions after annealing at 400°C (a); the onset of abnormal grain growth at 450°C (b); grain growth at 500°C (c) with corresponding diffraction pattern (d). Nanocrystalline α -Al and MgAl_2O_4 are indicated by the blue and red arcs, respectively.

3.6. Grain Size Stability. In cryomilled powders, there are two defined grain growth regimes, with the transition temperature T_c observed at $\sim 0.78T_m$ [1]. Below T_c the average grain size is fairly stable, but with increasing temperature the grain growth becomes more pronounced. T_c can be affected by many factors including solute impurities and highly stable nanoscale nitrides and oxides that are introduced into the powder during the milling process and are said to inhibit the mobility of the grain boundaries and prevent grain growth [5.1–5.5]. Previous studies on cryomilled Al systems and specifically Al-Mg and Al-Mg-Sc systems have shown these trends [1–5]. The Al-Mg-Er powder systems here show similar behavior. The 0.5 Er powder maintains the as-milled grain size up till $0.8T_m$ ($\approx 400^\circ\text{C}$), at which grain sizes are similar to those observed in the 0.1 Er composition and literature values for milled Al and Al-Mg powders.

3.6.1. Activation Energy for Grain Growth. In milled Al-Mg systems two sets of activation energies Q are typically reported, a lower Q for low temperature growth and at higher temperatures Q values closer to that of self or impurity diffusion in Al. In Tellkamp et al.'s study of a milled 5083 alloy powder, $Q \approx 5.6 \text{ kJ}\cdot\text{mol}^{-1}$ was reported for the low temperature regime ($T < 654 \text{ K}$), while $Q \approx 142 \text{ kJ}\cdot\text{mol}^{-1}$ was reported for the higher temperature regime ($T > 654 \text{ K}$) [4]. Another study on a bulk UFG 5083 alloy reported $Q = 25 \pm 5 \text{ kJ}\cdot\text{mol}^{-1}$ for the low temperature regime, while $Q = 124 \pm 5 \text{ kJ}\cdot\text{mol}^{-1}$ was found for higher temperatures ($T > 573 \text{ K}$) [5, 34]. Roy et al. [34] suggest that the low activation energy at low temperatures is indicative of highly unstable and nonequilibrium grain boundaries. Unstable grain boundaries could require smaller driving force for rearrangement of the grains and grain boundaries, while nonequilibrium boundaries may possess greater atomic mobility due to excess dislocations [34].

In order to determine the activation energy for the peak event (A), linear DSC scans are run at multiple heating rates from $5 \text{ K}\cdot\text{min}^{-1}$ to $40 \text{ K}\cdot\text{min}^{-1}$ under a flowing nitrogen atmosphere. The activation energy was determined using the KAS (Kissinger-Akahira-Sunose) method as described in [35] and shown as follows:

$$\ln\left(\frac{\beta}{T_f^\kappa}\right) = -\frac{E_a}{RT_f} + C, \quad (5)$$

where β is the heating rate used, T_f is the peak temperature of the event, E_a is the associated activation energy, R is the gas constant, C is a constant, and κ is a constant which is set to 1.95. The activation energies were determined as $Q_{0.1\text{Er}} = 18.0 \text{ kJ}\cdot\text{mol}^{-1}$ and $Q_{0.5\text{Er}} = 17.7 \text{ kJ}\cdot\text{mol}^{-1}$. The activation energies obtained here ($\approx 20 \text{ kJ}\cdot\text{mol}^{-1}$) are comparable with those found for the low temperature kinetic regime ($T < 600 \text{ K}$) and lie between the energies obtained for milled 5083 powder and bulk UFG 5083. The activation energy of $5.6 \text{ kJ}\cdot\text{mol}^{-1}$ was determined for milled 5083 powder where there is no strain relaxation. Similar to the findings of Roy et al. [34], the increase in activation energy of the Al-Mg-Er powders compared to the milled 5083 powder could be attributed to some strain relaxations taking place

with increased temperature. Annealing at 150°C resulted in limited grain growth in both powders (Figures 9 and 15) and reduced microstrain from the as-milled state (i.e., 0.041% in 0.1 Er and 0.066% in 0.5 Er). The microstructure and reduced microstrain, in addition to the low activation energies obtained, suggest a stress relaxation takes place in the low temperature regime ($\sim 150^\circ\text{C}$) that results in reduced strain in the material and reordered grain boundaries.

3.6.2. Er Effect on Grain Growth. Er addition to the Al-Mg system could potentially contribute to grain size control via either kinetic or thermodynamic means. In the work done by Murdoch and Schuh [36], their model generated moderate grain boundary segregation enthalpies for both Mg and La solutes ($0\text{--}25 \text{ kJ}\cdot\text{mol}^{-1}$) in a binary Al-based system, suggesting they could be effective as grain boundary stabilizers for a nanocrystalline Al matrix. If Er atoms have similar potential as La atoms in Al, the Er content could reduce the grain boundary energy and therefore reduce the driving force for grain growth. According to Darling et al. [37], true thermodynamic stabilization is defined by the reduction of grain boundary energy to zero. Based on this definition, the stability of binary systems based on various solute and solvent combinations is evaluated. According to their evaluations (for global concentrations less than 10 at.%), for the stabilization of a grain structure with 25 nm grains at $0.6T_m$ (396°C) in binary Al-based systems, Er is not a candidate for thermodynamic stabilization. Although the material systems studied here are more complex, consideration of the results of Darling et al. [37] and the Er content in the milled powders ($< 0.1 \text{ at.}\%$) suggest that Er does not contribute to a thermodynamic stability of the grain boundaries.

Considering kinetic effects on the grain growth, Er can contribute via either solute drag or second-phase pinning of grain boundaries by nanoscale Al_3Er phases. Both homogeneous and heterogeneous precipitation of Al_3Sc nanoscale phases were observed in cryomilled Al-7.5Mg-0.3Sc after annealing at 400°C for one hour, with precipitates approximately 5 nm in size observed within grains or along grain boundaries [5]. Compared to precipitation in Al-Sc alloys, the Al_3RE (Er, Yb) phase has been observed to have the tendency to nucleate heterogeneously due to the small chemical driving force for precipitation and to possess higher coarsening rates due to the higher diffusivities of RE atoms in Al and the larger $\alpha\text{-Al}/\text{Al}_3\text{RE}$ interfacial energy [38]. Therefore decomposition of the solid solution in this Al-Mg-Er nanocrystalline system should produce coarser precipitates of the Al_3Er phase. However, the absence of Li_2 phase reflections in the SAED patterns of the powders suggests the Er may remain in solute form in the powders and therefore contribute to the solute/impurity drag alongside with Mg and other impurity atoms.

3.6.3. Oxide Contributions to Grain Size Control. Due to the significant oxide content in the milled Al-Mg-Er powders, and their likely presence as nanoscale dispersoids, grain growth can be affected by second-phase pinning forces (i.e., $P_{\text{Zener}} = 3f\gamma/2r$) [5, 39]. Dispersoids formed in cryomilled

TABLE 6: Volume fraction of nanoscale oxides and Zener limit grain size.

Composition	Oxygen content (wt.%)	Oxide volume fraction, f	Grain size, D_{Zener} (nm)	Grain size below T_c (nm)
Milled Al alloys [13]	0.3–1.5	0.4–2.2	150	40
0.1 Er	8.4	12.7	27	37
0.5 Er	13	20.4	16	18

ODS Al powders during milling were reported as being aluminum oxynitride particles 2–10 nm in size [40] and platelets of aluminum-nitrogen and aluminum-oxygen content a few atomic layers thick and 10–15 nm in two dimensions [41]. If the volume fraction of the oxide is estimated by assuming the oxygen is present as oxide dispersoids and taking the average oxide/oxynitride particle to be 5 nm in size, it is possible to estimate the Zener limit grain size due to second-phase pinning forces. Table 6 shows the reported oxide content, equivalent estimated volume fraction of oxide and the Zener limit grain size ($D_{Zener} = 4r/3f$) for the 0.1 Er, 0.5 Er, and milled Al alloys. Up to 13 vol.% and 20 vol.% of nanoscale oxide particles could be present in the 0.1 Er and 0.5 Er powders, respectively, compared to the 2 vol.% in typical milled Al powders.

The Zener limit grain size D_{Zener} for both Al-Mg-Er milled powders matches well with the grain sizes observed after 1 h annealing below 450°C; this strongly supports the possibility of grain pinning by ultrafine particles. However, grain growth in milled Al-7.6 at.% Mg powder and 0.1 Er powder are almost identical despite the fact that there is a difference in oxygen content by more than a factor of 10 between both powders. Oxygen content in the Al-7.6 at.% Mg was reported as ~0.3 wt.% [3], while the 0.1 Er powder here contains 8 wt.% oxygen. From 100°C to 300°C, the grain size changes from 26 to 40 nm after 1 h annealing in Al-7.6 at.% Mg [3], almost identical to the grain size observed in the 0.1 Er powders changing from 23 nm at 150°C to 37 nm at 330°C. This shows that the grain size stability is not controlled by second-phase pinning alone, but likely from a combination of solute/impurity drag and second-phase pinning forces. However, for the 0.5 Er powder, maintenance of the as-milled grain size up to T_c is likely due to the increased oxide content, with grain growth at higher temperatures controlled by a combined solute and second-phase drag.

4. Conclusions

Atomized Al-Mg-Er powders, 0.1 Er and 0.5 Er, were cryogenically milled for 30 hours in liquid nitrogen. A supersaturated α -Al solid solution phase was obtained in both powders. Due to prolonged milling time, a substantial amount of oxygen contamination was observed in the final milled powders with 8.4 wt.% and 13 wt.% oxygen detected in the 0.1 Er and 0.5 Er powders, respectively. The thermal stability of the microstructure was investigated by DSC; isothermal annealing at selected temperatures was followed by XRD and TEM analyses. The DSC traces exhibited a recovery event at ~160°C. An activation energy of ~20 kJ·mol⁻¹ was determined for the recovery event in both powders by the KAS method using heating rates of 5–40 K·min⁻¹. This is similar to

activation energies reported for the low temperature regime in milled 5083 material and attributed to the presence of highly unstable and nonequilibrium grain boundaries.

Overall thermal stability in the Al-Mg-Er powders was attributed to the combined effects of solute/impurity drag and second-phase pinning (nanoscale oxides, nitrides, and oxynitrides) that impede grain boundary motion. The 0.1 Er powder exhibited grain growth behavior similar to other milled Al-Mg powders reported in literature, with abnormal grain growth observed after annealing at 180°C. The 0.5 Er powder showed improved thermal stability at low temperatures with as-milled grain size of ~20 nm maintained till 400°C ($0.8T_m$). Controlled grain growth at higher temperatures resulted in an average grain size of 55 nm and a maximum observed grain size of ~200 nm after one hour of annealing at 500°C.

Second-phase particles of Al-Mg-O (~40 nm) and Al-Fe (~80 nm) were observed in the annealed 0.1 Er powders by STEM analysis. SAED patterns from powders annealed at 180°C, 330°C, and 500°C could be indexed to nanocrystalline MgO phases. Crystalline spinel phases were detected by XRD in powders annealed at temperatures of 500°C and higher. Detection of nitrogen-containing particles was not possible due to limitations of the equipment used; however, it is highly likely that nanoscale dispersoids of oxynitrides are also present in the milled powders. Evidence of nanoscale $L1_2$ Al_3Er precipitation was not found in either powder composition.

Conflicts of Interest

The authors declare that there are no conflicts of interest regarding the publication of this paper.

Acknowledgments

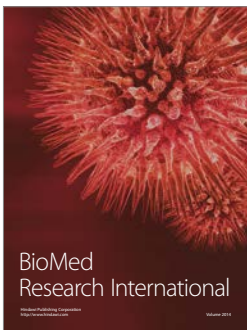
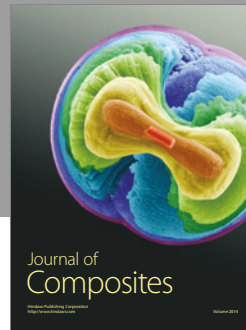
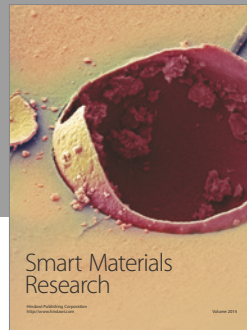
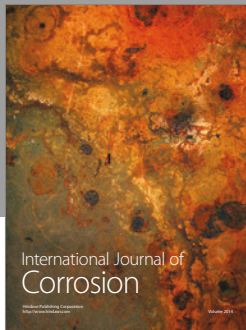
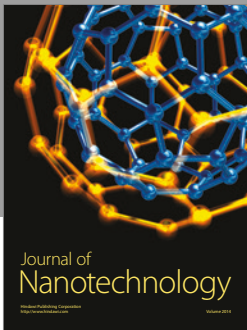
The authors would like to thank Nicolas Brodusch and David Liu for their assistance with electron microscopy imaging. Funding for the project was provided by FQRNT.

References

- [1] F. Zhou, J. Lee, and E. J. Lavernia, "Grain growth kinetics of a mechanically milled nanocrystalline Al," *Scripta Materialia*, vol. 44, no. 8-9, pp. 2013–2017, 2001.
- [2] F. Zhou, J. Lee, S. Dallek, and E. J. Lavernia, "High grain size stability of nanocrystalline Al prepared by mechanical attrition," *Journal of Materials Research*, vol. 16, no. 12, pp. 3451–3458, 2001.
- [3] F. Zhou, X. Z. Liao, Y. T. Zhu, S. Dallek, and E. J. Lavernia, "Microstructural evolution during recovery and recrystallization of a nanocrystalline Al-Mg alloy prepared by cryogenic ball milling," *Acta Materialia*, vol. 51, no. 10, pp. 2777–2791, 2003.

- [4] V. L. Tellkamp, S. Dallek, D. Cheng, and E. J. Lavernia, "Grain growth behavior of a nanostructured 5083 Al-Mg alloy," *Journal of Materials Research*, vol. 16, no. 4, pp. 938–944, 2001.
- [5] F. Zhou, Z. Lee, E. J. Lavernia, and S. R. Nutt, "The influence of Sc on thermal stability of a nanocrystalline Al-Mg alloy processed by cryogenic ball milling," *Metallurgical and Materials Transactions A*, vol. 36, no. 6, pp. 1587–1594, 2005.
- [6] J. Røyset and N. Ryum, "Scandium in aluminium alloys," *International Materials Reviews*, vol. 50, no. 1, pp. 19–44, 2005.
- [7] Chemicool Periodic Table, 2017, <http://www.chemicool.com/>.
- [8] G.-F. Xu, S.-Z. Mou, J.-J. Yang, T.-N. Jin, Z.-R. Nie, and Z.-M. Yin, "Effect of trace rare earth element Er on Al-Zn-Mg alloy," *Transactions of Nonferrous Metals Society of China*, vol. 16, no. 3, pp. 598–603, 2006.
- [9] S. P. Wen, Z. B. Xing, H. Huang, B. L. Li, W. Wang, and Z. R. Nie, "The effect of erbium on the microstructure and mechanical properties of Al-Mg-Mn-Zr alloy," *Materials Science and Engineering A*, vol. 516, no. 1-2, pp. 42–49, 2009.
- [10] M. Gang, L. bolong, L. hongmei, H. hui, and N. zuoren, "Hot deformation behavior of an Al-5.7 wt.% Mg alloy with erbium," *Materials Science and Engineering A*, vol. 516, no. 1-2, pp. 131–137, 2009.
- [11] S. Lin, Z. Nie, H. Huang, and B. Li, "Annealing behavior of a modified 5083 aluminum alloy," *Materials and Design*, vol. 31, no. 3, pp. 1607–1612, 2010.
- [12] R. A. Varin, J. Bystrzycki, and A. Calka, "Effect of annealing on the microstructure, ordering and microhardness of ball milled cubic (L_{12}) titanium trialuminide intermetallic powder," *Intermetallics*, vol. 7, no. 7, pp. 785–796, 1999.
- [13] D. B. Witkin and E. J. Lavernia, "Synthesis and mechanical behavior of nanostructured materials via cryomilling," *Progress in Materials Science*, vol. 51, no. 1, pp. 1–60, 2006.
- [14] J. Zhang, J. J. Zhao, and R. L. Zuo, "Microstructure and mechanical properties of micro-alloying modified Al-Mg alloys," in *Proceedings of the International Conference on Power Electronics and Energy Engineering (PEEE '15)*, pp. 153–156, Hong Kong, China, April 2015.
- [15] H. Okamoto, "Al-Mg (aluminum-magnesium)," *Journal of Phase Equilibria*, vol. 19, no. 6, pp. 598–598, 1998.
- [16] C. Goujon, P. Goeuriot, P. Delcroix, and G. Le Caër, "Mechanical alloying during cryomilling of a 5000 Al alloy/AlN powder: the effect of contamination," *Journal of Alloys and Compounds*, vol. 315, no. 1-2, pp. 276–283, 2001.
- [17] S. Scudino, M. Sakaliyska, K. B. Surreddi, and J. Eckert, "Mechanical alloying and milling of Al-Mg alloys," *Journal of Alloys and Compounds*, vol. 483, no. 1-2, pp. 2–7, 2009.
- [18] F. Zhou, D. Witkin, S. R. Nutt, and E. J. Lavernia, "Formation of nanostructure in Al produced by a low-energy ball milling at cryogenic temperature," *Materials Science and Engineering A*, vol. 375–377, no. 1-2, pp. 917–921, 2004.
- [19] F. Zhou, S. R. Nutt, C. C. Bampton, and E. J. Lavernia, "Nanostructure in an Al-Mg-Sc alloy processed by low-energy ball milling at cryogenic temperature," *Metallurgical and Materials Transactions A*, vol. 34, no. 9, pp. 1985–1992, 2003.
- [20] D. Briggs and M. P. Seah, *Practical Surface Analysis*, vol. 1, John Wiley & Sons Ltd, Chichester, UK, 2nd edition, 1990.
- [21] L. P. H. Jeurgens, W. G. Sloof, F. D. Tichelaar, C. G. Borsboom, and E. J. Mittemeijer, "Determination of thickness and composition of aluminium-oxide overlayers on aluminium substrates," *Applied Surface Science*, vol. 144–145, no. 0, pp. 11–15, 1999.
- [22] M. R. Alexander, G. E. Thompson, X. Zhou, G. Beamson, and N. Fairley, "Quantification of oxide film thickness at the surface of aluminium using XPS," *Surface and Interface Analysis*, vol. 34, no. 1, pp. 485–489, 2002.
- [23] M. Schoenitz and E. Dreizin, "Oxidation processes and phase changes in metastable Al-Mg alloys," *Journal of Propulsion and Power*, vol. 20, no. 6, pp. 1064–1068, 2004.
- [24] D. J. Field, G. M. Scamans, and E. P. Butler, "The high temperature oxidation of Al-4.2 wt pct Mg alloy," *Metallurgical Transactions A*, vol. 18, no. 4, pp. 463–472, 1987.
- [25] P.-C. Chen, T.-S. Shih, and C.-Y. Wu, "Thermally formed oxides on Al-2 and 3.5 mass% Mg alloys heated and held in different gases," *Materials Transactions*, vol. 50, no. 10, pp. 2366–2372, 2009.
- [26] B. B. Straumal, B. Baretzky, A. A. Mazilkin et al., "Formation of nanograin structure and decomposition of supersaturated solid solution during high pressure torsion of Al-Zn and Al-Mg alloys," *Acta Materialia*, vol. 52, no. 15, pp. 4469–4478, 2004.
- [27] X. Sauvage, N. Enikeev, R. Valiev, Y. Nasedkina, and M. Murashkin, "Atomic-scale analysis of the segregation and precipitation mechanisms in a severely deformed Al-Mg alloy," *Acta Materialia*, vol. 72, pp. 125–136, 2014.
- [28] G. K. Rane, D. Apel, U. Welzel, and E. J. Mittemeijer, "The microstructural evolution and thermal stability of nanocrystalline ball-milled Ni-15 at.% W powder," *Journal of Materials Research*, vol. 28, no. 6, pp. 873–886, 2013.
- [29] E. A. Marquis and D. N. Seidman, "Nanostructural evolution of Al_3Sc precipitates in an Al-Sc-Mg alloy by three-dimensional atom probe microscopy," *Surface and Interface Analysis*, vol. 36, no. 5-6, pp. 559–563, 2004.
- [30] M. J. Starink and A.-M. Zahra, "Low-temperature decomposition of Al-Mg alloys: Guinier-preston zones and L_{12} ordered precipitates," *Philosophical Magazine A*, vol. 76, no. 3, pp. 701–714, 1997.
- [31] M. J. Starink and A.-M. Zahra, " β' and β precipitation in an Al-Mg alloy studied by DSC and TEM," *Acta Materialia*, vol. 46, no. 10, pp. 3381–3397, 1998.
- [32] T. J. Harrell, T. D. Topping, H. Wen, T. Hu, J. M. Schoenung, and E. J. Lavernia, "Microstructure and strengthening mechanisms in an ultrafine grained Al-Mg-Sc alloy produced by powder metallurgy," *Metallurgical and Materials Transactions A*, vol. 45, no. 13, pp. 6329–6343, 2014.
- [33] L. Shaw, H. Luo, J. Villegas, and D. Miracle, "Thermal stability of nanostructured $Al_{93}Fe_3Cr_2Ti_2$ alloys prepared via mechanical alloying," *Acta Materialia*, vol. 51, no. 9, pp. 2647–2663, 2003.
- [34] I. Roy, M. Chauhan, E. J. Lavernia, and F. A. Mohamed, "Thermal stability in bulk cryomilled ultrafine-grained 5083 Al alloy," *Metallurgical and Materials Transactions A*, vol. 37, no. 3, pp. 721–730, 2006.
- [35] M. J. Starink, "Analysis of aluminium based alloys by calorimetry: quantitative analysis of reactions and reaction kinetics," *International Materials Reviews*, vol. 49, no. 3-4, pp. 191–226, 2004.
- [36] H. A. Murdoch and C. A. Schuh, "Estimation of grain boundary segregation enthalpy and its role in stable nanocrystalline alloy design," *Journal of Materials Research*, vol. 28, no. 16, pp. 2154–2163, 2013.
- [37] K. A. Darling, M. A. Tschopp, B. K. Vanleeuwen, M. A. Atwater, and Z. K. Liu, "Mitigating grain growth in binary nanocrystalline alloys through solute selection based on thermodynamic stability maps," *Computational Materials Science*, vol. 84, pp. 255–266, 2014.

- [38] M. E. van Dalen, R. A. Karnesky, J. R. Cabotaje, D. C. Dunand, and D. N. Seidman, "Erbium and ytterbium solubilities and diffusivities in aluminum as determined by nanoscale characterization of precipitates," *Acta Materialia*, vol. 57, no. 14, pp. 4081–4089, 2009.
- [39] C. S. Smith, "Grains, phases and interfaces: an interpretation of microstructure," *Transactions of AIME*, vol. 175, pp. 15–51, 1948, <https://link.springer.com/article/10.1007%2Fs11661-010-0215-5>.
- [40] M. J. Luton, C. S. Jayanth, M. M. Disko, S. Matras, and J. Vallone, "Cryomilling of nano-phase dispersion strengthened aluminum," *MRS Proceedings*, vol. 132, pp. 79–86, 1988.
- [41] O. Susegg, E. Hellum, A. Olsen, and M. J. Luton, "HREM study of dispersoids in cryomilled oxide dispersion strengthened materials," *Philosophical Magazine A*, vol. 68, no. 2, pp. 367–380, 1993.



Hindawi

Submit your manuscripts at
<https://www.hindawi.com>

